NANO LETTERS
Letter
Cite This: Nano Lett. 2019, 19, 4551−4559
pubs.acs.org/NanoLett

Quasi-2D Transport and Weak Antilocalization Effect in Few-layered VSe_2

Hongtao Liu,[†,#] Lihong Bao,*[,†,‡,#] Zhang Zhou,[†] Bingyu Che,[†] Ruizi Zhang,[†] Ce Bian,[†] Ruisong Ma,[†] Liangmei Wu,[†] Haifang Yang,[†] Junjie Li,[†] Changzhi Gu,[†] Cheng-Min Shen,[†,‡] Shixuan Du,[†,‡] and Hong-Jun Gao[†]

[†]Institute of Physics & University of Chinese Academy of Sciences, Chinese Academy of Sciences, Beijing, 100190, P. R. China
[‡]Songshan Lake Materials Laboratory, Dongguan, Guangdong 523808, P. R. China

Supporting Information

ABSTRACT: With strong spin−orbit coupling (SOC), ultrathin two-dimensional (2D) transitional metal chalcogenides (TMDs) are predicted to exhibit weak antilocalization (WAL) effect at low temperatures. The observation of WAL effect in VSe_2 is challenging due to the relative weak SOC and three-dimensional (3D) transport nature in thick VSe_2. Here, we report on the observation of quasi-2D transport and WAL effect in sublimed-salt-assisted low-temperature chemical vapor deposition (CVD) grown few-layered high-quality VSe_2 nanosheets. The WAL magnitudes in magnetoconductance can be perfectly fitted by the 2D Hikami−Larkin−Nagaoka (HLN) equation in the presence of strong SOC, by which the spin−orbit scattering length l_{SO} and phase coherence length l_ϕ have been extracted. The phase coherence length l_ϕ shows a power law dependence with temperature, $l_\phi \sim T^{-1/2}$, revealing an electron−electron interaction-dominated dephasing mechanism. Such sublimed-salt-assisted growth of high-quality few-layered VSe_2 and the observation of WAL pave the way for future spintronic and valleytronic applications.

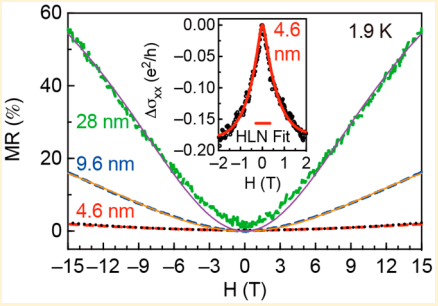

KEYWORDS: *VSe_2, sublimed-salt-assisted chemical vapor deposition, spin−orbit coupling, weak antilocalization effect, electron−electron interactions*

Spin−orbit coupling (SOC) plays a crucial role in the spin-Hall effect and topological states in condensed matter systems.[1] It leads to degenerated valley-locked spin-split in monolayer transition metal dichalcogenides (TMDs) with broken inversion symmetry, which enables the use of spin and valley as information carriers.[2] Furthermore, SOC in two-dimensional (2D) materials can be effectively tuned by electrostatic gate fields, making 2D materials ideal platforms for next generation spintronics and valleytronics.[3−5] To selectively manipulate the individual valley, the degeneracy of the two valleys (K_+ and K_-) should be lifted.[6−9] Calculations and experiments have demonstrated that monolayer VSe_2 is ferromagnetic, which persists even at room temperature.[10−12] The ferromagnetic order in monolayer VSe_2 breaks not only the inversion symmetry but also the time reversal symmetry. As a consequence, the degeneracy of the K_+ and K_- valleys in the Brillouin zone protected by time-reversal symmetry is broken, which makes it intrinsically valley-polarized induced by SOC.[13,14] This offers VSe_2 an easily accessible valley degree of freedom for its promising applications in future electronics. In the presence of strong SOC, weak antilocalization (WAL) effect will emerge.[15,16] WAL effect is a quantum correction to the magnetoconductance that comes from the destructive interference between pairs of time-reversed trajectories of electrons elastically scattering in a closed loop in the presence of SOC. It decreases the probability of charge-carrier backscattering in a conductor in the diffusive regime and thus enhances the conductance.[15,17] WAL was observed in 2D TMDs with large atomic numbers due to strong SOC, such as WTe_2,[18−21] $MoTe_2$,[22] WSe_2,[3] $TaSe_2$,[23] and $PtTe_2$.[24] However, observation of WAL in TMD materials composed of light atoms, such as MoS_2, is challenging due to the relative weak SOC. It is only achieved under restrict conditions, such as at very low temperature or applying a gate voltage.[25,26] The enhancement of WAL by the quantum confinement in 2D limit makes the observation of WAL effect possible in monolayer and few-layer TMD materials.[27,28] Bulk VSe_2 exhibits a 3D warping of the Fermi surface and concomitant nesting as the precursor for the formation of 3D charge-density waves (CDWs) revealed by angle-resolved photoemission spectroscopy (ARPES).[29,30] Electrical transport measurement on bulk VSe_2 also shows its 3D transport nature with a CDW transition at temperature $T_{CDW} \approx 110$ K.[31] Even for the 11 nm thick VSe_2 nanosheets, the 3D transport characteristics still persisted.[32] Furthermore, the difficulty in preparation of ultrathin high-quality VSe_2 makes the transport study of the

Received: April 5, 2019
Revised: June 24, 2019
Published: June 25, 2019

DOI: 10.1021/acs.nanolett.9b01412
Nano Lett. 2019, 19, 4551−4559

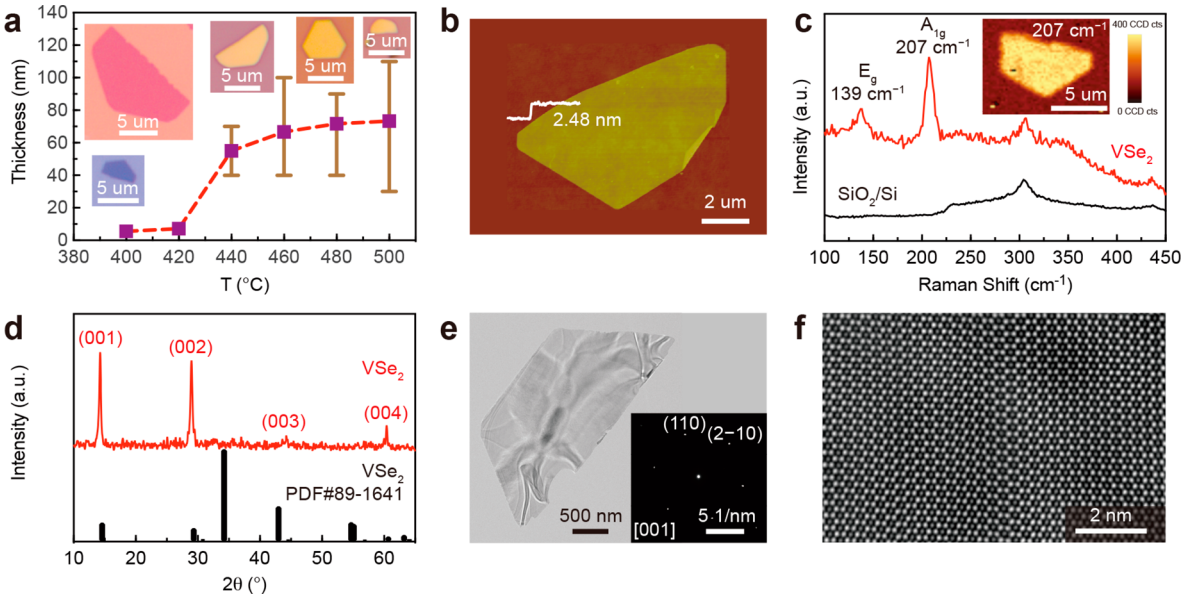

Figure 1. Thickness-controlled CVD synthesis of high-quality VSe_2 nanosheets. (a) Thickness of VSe_2 nanosheets as a function of growth temperature. Insets are typical optical images of VSe_2 nanosheets on SiO_2/Si substrates. (b) AFM image and corresponding height profile of a 2.48 nm thick VSe_2 nanosheet grown at 400 °C. (c) Raman spectrum of a 4.2 nm thick VSe_2 nanosheet with E_g peak at ~139 cm^{-1} and A_{1g} peak at ~207 cm^{-1}. Inset shows Raman mapping of A_{1g} peak at ~207 cm^{-1}. (d) XRD patterns of as-grown VSe_2 nanosheets along with the standard powder diffraction file (PDF) for 1T phase VSe_2. (e) Low-magnification transmission electron microscope (TEM) image of a VSe_2 nanosheet. Inset shows the selected-area electron diffraction (SAED) pattern of the VSe_2 nanosheet. (f) High-angle annular dark-field scanning TEM (HAADF-STEM) image of VSe_2 with atomic resolution (filtered).

relatively weak intrinsic SOC in VSe_2 by WAL effect and other physical properties a challenge.

Here we have successfully prepared high-quality VSe_2 nanosheets with tunable thickness from tens of nanometers to 2.48 nm (about 4 layers, 4L) by a sublimed-salt-assisted atmospheric pressure chemical vapor deposition (CVD) method at low growth temperature. The capability of tuning thickness of VSe_2 nanosheets allows for the measurement of thickness-dependent transport and the observation of WAL effect in few-layered VSe_2 nanosheets. The highly crystalline nature of VSe_2 nanosheets is confirmed by Raman spectroscopy, X-ray photoemission spectroscopy (XPS), and scanning transmission electron microscopy (STEM). All VSe_2 nanosheets, with thickness down to 4.6 nm (~7L), are metallic with large residual resistivity ratio (RRR, RRR = $\rho_{300\ K}/\rho_{2\ K}$, largest RRR ≈ 37) and exhibit monotonic decreasing CDW transition temperatures with decreasing thickness. No resistivity upturn caused by disorder-induced weak localization or Kondo effect is observed for thick samples (>5 nm) at low temperatures.[33,34] While for VSe_2 nanosheets thinner than 5 nm, the resistivity upturn emerges at low temperature, which is due to the electron−electron (e−e) interactions. Large positive and linear magnetoresistance (MR) is observed in thick VSe_2 nanosheets at temperature below T_{CDW}, which is suppressed with decreasing thickness. WAL effect, as a hallmark of SOC, is observed in a 4.6 nm thick (~7L) few-layered VSe_2 nanosheet at temperatures below 10 K. The magnetoconductance due to WAL effect is analyzed using the Hikami−Larkin−Nagaoka (HLN) equation, and an e−e interaction dephasing mechanism is revealed.

VSe_2 nanosheets were grown on SiO_2/Si or sapphire substrates by a sublimed-salt-assisted CVD method (see Methods and Supporting Information). Ammonium chloride (NH_4Cl) was used as a growth promoter to grow high quality few-layer VSe_2 nanosheets. It sublimes and decomposes into gas species, which are transported by carrier gas during the growth process. High quality VSe_2 nanosheets without salt contamination can be produced at low growth temperature. The thickness of VSe_2 nanosheets can be modulated from ~2.48 nm (~4L) to tens of nanometers by simply adjusting the growth temperature in the range from 500 to 400 °C, as shown in Figure 1a. The thickness of VSe_2 nanosheets can also be roughly identified by its color on SiO_2/Si substrate, as thin VSe_2 nanosheets (<10 nm) show dark purple color while thick nanosheets (>50 nm) show apparently metallic luster (Figures 1a and S1b). The exact thickness of VSe_2 nanosheets was measured by atomic force microscopy (AFM), and the thinnest nanosheet was 2.48 nm (~4L), which was obtained by the line profile of the AFM image, as shown in Figure 1b.

The VSe_2 nanosheets were first confirmed by Raman spectroscopy. Two prominent peaks at 207 and 139 cm^{-1} in the Raman spectrum of VSe_2 nanosheets are corresponding to the out-of-plane A_{1g} mode and the in-plane E_g mode of 1T phase VSe_2, respectively (Figure 1c).[35,36] Raman mapping at A_{1g} mode shows a uniform contrast in the inset of Figure 1c, indicating a uniform crystal structure across the entire VSe_2 nanosheet. No oxidation peak at about 250 cm^{-1} in the as-grown VSe_2 nanosheets are observed, which will appear if the VSe_2 nanosheet is irradiated under large laser power during collecting the Raman signals or exposed to ambient condition for over about 1 week (Figure S5).[37] There is a slight shift of the E_g mode compared to that of the thick VSe_2, which is observed at 143 cm^{-1} and is small and broad at low temperature.[35] The observation of the E_g mode at room temperature may be due to the high-quality few-layer thickness of the VSe_2 nanosheets and the use of small laser power (<1 mW) when collecting the Raman signals. However, the E_g mode blurs in thick VSe_2 nanosheet or in nanosheets degraded

DOI: 10.1021/acs.nanolett.9b01412
Nano Lett. 2019, 19, 4551−4559

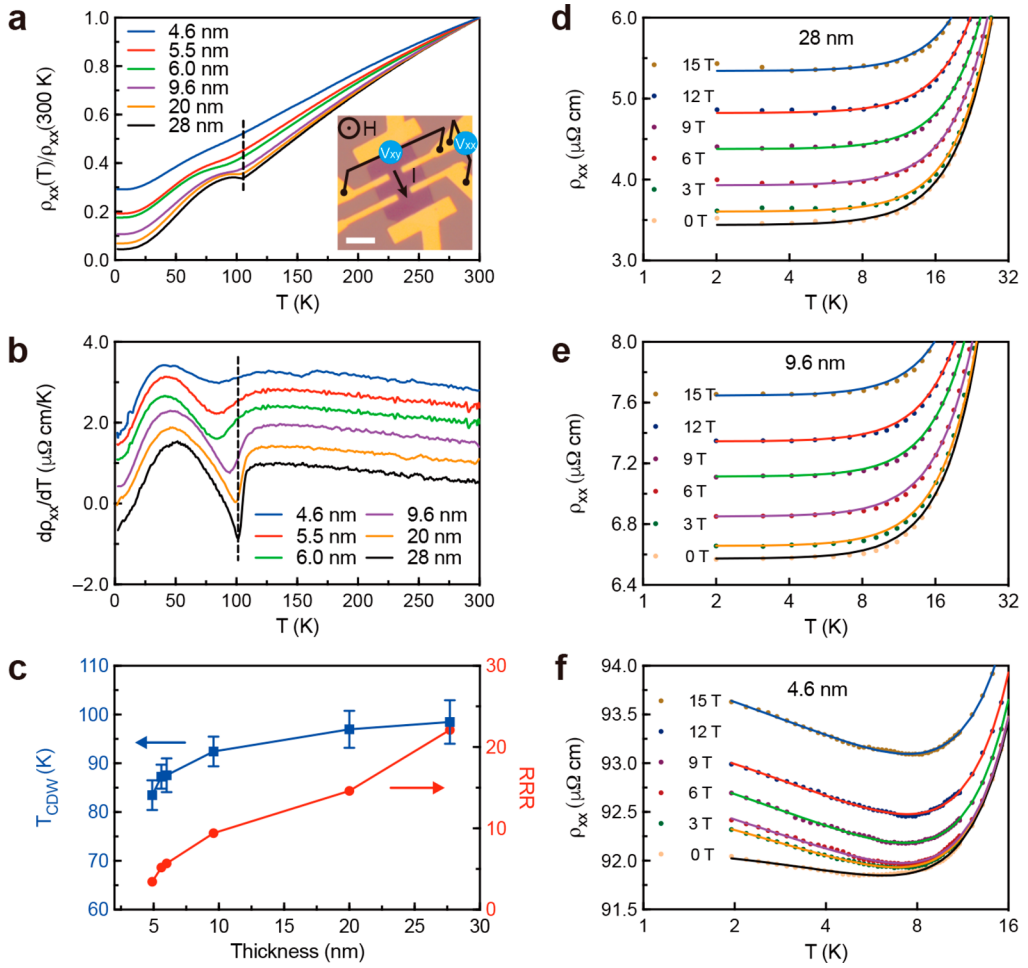

Figure 2. Temperature dependence of longitudinal resistivity of VSe_2 nanosheets with different thickness. (a) Temperature-dependent longitudinal resistivity (normalized) and (b) first derivative of the resistivity of VSe_2 nanosheets with different thickness, respectively. The charge-density wave (CDW) transition temperature (T_{CDW}) is defined by at which temperature the first derivative of resistivity reaches the minimum. Inset in (a) is the optical image of the Hall bar device of the 9.6 nm thick VSe_2 nanosheet and schematic diagram of measurement configuration of the device. Scale bar, 5 μm. Offset in (b) for clearance. Dashed lines in (a) and (b) are guidelines of the T_{CDW} of the 28 nm VSe_2 nanosheet. (c) Thickness dependence of T_{CDW} and residual resistivity ratio (RRR = $\rho_{300\ K}/\rho_{2\ K}$). Logarithmic temperature dependence of resistivity of the VSe_2 nanosheets with the thickness of (d) 28, (e) 9.6, and (f) 4.6 nm under different magnetic fields at low temperatures, respectively. Solid dots indicate experimental data points, and solid lines in (d) and (e) are fitting results by $\rho \propto T^3$. Resistivity upturn at low temperature appears in the 4.6 nm thick sample. The solid lines in (f) are fittings based on $\rho \propto T^3$ and quantum corrections due to weak antilocalization (WAL) effect and electron−electron (e−e) interactions (see main text).

by larger laser power or exposure to air for a long time (Figure S5). It is quite different from the excellent stability of thicker samples.[36] In short, the E_g peak is temperature, thickness, and quality sensitive and can be used as a hallmark of high-quality few-layer thick VSe_2 nanosheets. The 1T phase of VSe_2 nanosheets is also confirmed by X-ray diffraction (XRD, Figure 1d).

The high quality of the VSe_2 nanosheets is further validated by TEM. Figure 1e is the low magnification TEM image of a typical VSe_2 nanosheet. Energy-dispersive X-ray spectroscopy (EDS) mapping demonstrates that V and Se elements are uniformly distributed in the whole nanosheet (Figure S4b,c). Elementary analysis (Figure S4d) of the nanosheet by EDS reveals that there are no other impurity elements except Se and V in the sample with the atomic ratio of Se/V = 69.83/30.17 ≈ 2.3, which is very close to the stoichiometric ratio in VSe_2. The larger atomic ratio may be due to the adsorbed Se during growth.[34] The copper signals originate from the copper TEM grid. One set of selected-area electron diffraction (SAED) patterns at different locations are shown in Figures 1e and S4e,f, demonstrating the single crystalline and 1T phase of the VSe_2 nanosheet. Atomic-resolution high-angle annular dark-field scanning transmission electron microscope (HAADF-STEM) image in Figure 1f shows no defects in all the examined regions of the VSe_2 nanosheet, indicating the high quality of the sample.

Taking advantage of the thickness-tunable growth and the high quality of VSe_2 nanosheets, thickness-dependent magnetotransport was performed on Hall-bar devices fabricated by a standard electron beam lithography technique (see Methods and Figure S8). Due to the poor contrast and small lateral size of thinner VSe_2 nanosheets on SiO_2/Si substrate, the thinnest nanosheet to fabricate a device was 4.6 nm, though the thinnest VSe_2 nanosheet grown was 2.48 nm. Temperature-dependence of resistivity ($\rho-T$) of VSe_2 nanosheets with different thickness are shown in Figures 2, S9, S12, and S13. We focused on the VSe_2 nanosheets with thickness of 28, 9.6, and 4.6 nm to study the transport behavior of bulk-like,

DOI: 10.1021/acs.nanolett.9b01412
Nano Lett. 2019, 19, 4551−4559

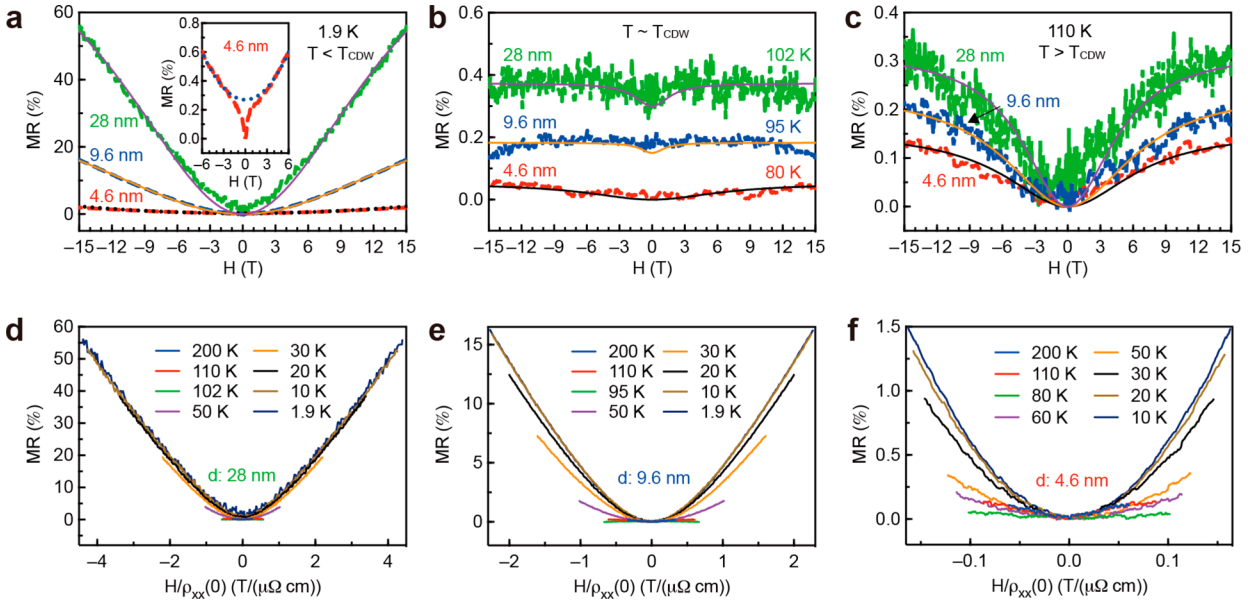

Figure 3. Magnetoresistance (MRs) of VSe_2 nanosheets with different thickness. (a−c) MRs of the 28, 9.6, and 4.6 nm thick VSe_2 nanosheets at different temperatures: (a) at 1.9 K, below T_{CDW}, (b) at temperatures around T_{CDW}, and (c) at 110 K, above T_{CDW}. Dashed lines are experimental data, and solid lines are fitting results by the two-band model. Quadratic fitting of MR of the 4.6 nm thick VSe_2 nanosheet at 1.9 K in the magnetic field range of ±3 to ±8 T is shown by dotted lines in inset of (a). The dip in low field at 1.9 K in (a) indicating the WAL effect. (d−f) Kohler's plot of MRs of the 28, 9.6, and 4.6 nm thick VSe_2 nanosheets, respectively.

intermediate thick, and thinnest nanosheets, respectively. All VSe_2 nanosheets show metallic behavior regardless of the different thickness. The largest RRR is about 37 (Figure S13a), and the average RRR is about 20 for thick VSe_2 nanosheets (~10 nm). The RRR of VSe_2 is almost the largest among the samples prepared by chemical vapor transport and other CVD method,[31,32,36] which demonstrates the high quality of our sample with fewer impurities and crystallographic defects. The electrical conductivity is about 1.6×10^6 S m^{-1} at 300 K and increases an order of magnitude to about 1.5×10^7 S m^{-1} at 2 K, both are larger than the best value of VSe_2.[36] There is negligible hysteresis in the cooling and warming cycles, indicating the uneven heating and absence of extra vanadium (Figure S9a,c,e).[31] In high temperature range (~110 to ~200 K), the resistivity varies linearly with temperature ($\rho \propto T$) due to phonon scattering,[38] indicated by the dash lines fitted to equation:

$$\rho(T) = \rho_{ti} + AT \quad (1)$$

in which the first term ρ_{ti} is the temperature-independent resistivity and the second term is due to the electron−phonon (e−ph) interactions (Figure S9b,d,f). The corresponding coefficients ρ_{ti} and A are shown in Table S2. The kink at about 100 K is caused by CDW transition.[32,38,39] As shown in Figure 2a, with the thickness decreasing, the kinks in the $\rho-T$ curves become obscure, which could be induced by either the reduced dimensionality, or degraded quality due to slight oxidation of the thin nanosheets, or Coulombic scattering from the substrate.[32,37,38,40] The CDW transition temperature T_{CDW} is defined at the point where the minimum occurs in the first derivative of the $\rho-T$ curve (Figure 2b).[32,36] As the thickness of VSe_2 nanosheets decreases from 28 to 4.6 nm, the RRR and T_{CDW} reduce from 21.99 to 3.42 and from 101.6 to 85.67 K, respectively (Figure 2c). The thickness-dependent T_{CDW} is consistent with previous results in the literature, indicating that the 3D interlayer coupling favors the CDW state in VSe_2 and the suppression of CDW in thinner VSe_2 nanosheets down to 4.6 nm (~7L).[32]

At low temperatures, no resistivity upturn is observed in thick samples (>5 nm, Figures 2d,e, S9a,c, S12c,e, and S13a), suggesting no defects-induced weak localization (WL) present in thick VSe_2 nanosheets.[33] At the temperatures ranging from 2 to 30 K, the $\rho-T$ curves can be well fitted by the following equation (Figure 2d,e):

$$\rho(T) = \rho_0 + BT^3 \quad (2)$$

in which the first term is residual resistivity, the second term is due to e−ph interactions. The parameters ρ_0 and B are listed in Table S3. The T^3 dependence of e−ph interactions is in good agreement with ref 34 and may be due to the two-band transport.[31] While for the 4.6 nm thick VSe_2 nanosheet, an upturn in resistivity at temperature below 10 K emerges (Figure 2f), the low-temperature resistivity minimum usually originates from e−e interactions, WL, or Kondo effect.[33,34] However, WL and Kondo effect will be suppressed by perpendicular magnetic field.[15] The $\rho-T$ curves of the 4.6 nm thick VSe_2 nanosheets under different perpendicular magnetic fields are shown in Figure 2f. It is apparent that the resistivity upturn is not suppressed but instead enhanced by magnetic fields, as shown in Figure 2f. Therefore, the WL and Kondo effect can be safely ruled out, and the upturn in resistivity at low temperatures is resulting from e−e interactions, which is not affected by magnetic field.[41] This is consistent with the theoretical predictions that reduced dimension will enhance the e−e interactions and that a metal−insulator transition will appear in monolayer VSe_2.[42] The contribution of e−e interactions to the resistivity is logarithmically dependent on the temperature in the case of two dimensions (2D) and shows power law dependence in three dimensions (3D).[17] All the $\rho-T$ curves at temperature below 15 K shown in Figure 2f can be well fitted by equation:

DOI: 10.1021/acs.nanolett.9b01412
Nano Lett. 2019, 19, 4551−4559

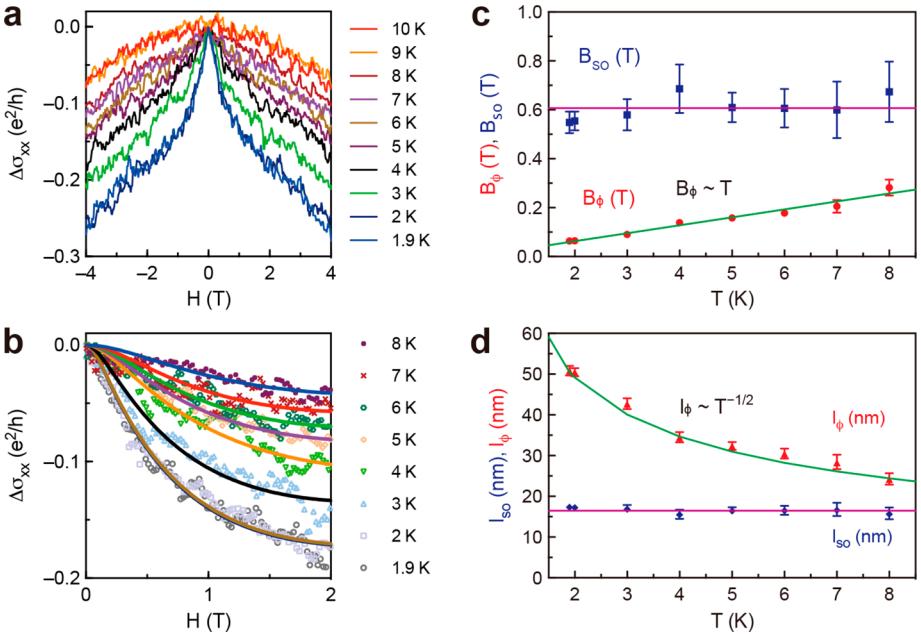

Figure 4. Weak antilocalization effect and electron dephasing in the 4.6 nm thick VSe_2 nanosheet. (a) Magnetoconductance $\Delta\sigma_{xx}$ as a function of applied low perpendicular magnetic field at temperatures below 10 K. (b) Magnetic field dependence of magnetoconductances (symbols) below 10 K along with the best fit (solid lines) to the weak localization theory of Hikami, Larkin and Nagaoka (HLN). (c) Temperature dependence of characteristic dephasing field B_ϕ and spin−orbit scattering field B_{SO} extracted from the HLN fitting. The solid green line is the fit to $B_\phi \propto T^p$ with $p = 1$, indicating the dephasing is caused by Nyquist e−e interactions. The solid magenta line is the guide line showing the temperature independence of B_{SO}. (d) Temperature dependence of phase coherence length l_ϕ and spin−orbit scattering length l_{SO}, extracted from the equation $B_{\phi,SO} = \hbar/(4el^2_{\phi,SO})$. The solid green line is the fit to $l_\phi \propto T^{-1/2}$ and the solid magenta line is the guide line.

$$\rho(T) = \rho_0 + BT^3 - C\ln(T) - DT^{1/2} \quad (3)$$

where the first term is residual resistivity, the second term is e−ph contribution, the third term is the contribution from 2D e−e interactions, and the forth term is 3D e−e interactions.[17] The fitting parameters ρ_0, B, C, and D are listed in Table S4. The perfect fits to eq 3 indicate that with the reduction of thickness in VSe_2 nanosheets, 2D transport emerges. The 3D nature of electronic structure in bulk VSe_2 is revealed in previous ARPES measurement,[30] which is also verified by our density function theoretical calculations (Figure S14). The emergence of 2D transport highlights the role of quantum confinement effect with the reduction of thickness in VSe_2 nanosheets. However, for the 4.6 nm thick VSe_2 nanosheet, the 3D transport is still presented, resulting in a quasi-2D transport behavior.

Transverse MR, defined as $[\rho(H) - \rho(0)]/\rho(0) \times 100\%$, of the VSe_2 nanosheets with different thickness at various temperatures was measured by applying a magnetic field parallel to the c axis of the VSe_2 nanosheet and perpendicular to the current direction (Figures 3, S10, S12, and S13). As shown in Figure 3a, the MR is quadratically dependent on the magnetic field at low fields and linear at high fields at 1.9 K. The MR amplitudes and the crossover fields are about 55.8% and 2.4 T, 16.2% and 5.5 T, and 1.94% and 9 T for the VSe_2 nanosheets with thickness of 28, 9.6, and 4.6 nm, respectively. These results indicate that, with decreasing thickness, MR amplitude is decreased, while the crossover field is increased. The largest linear MR is 50% in a ~ 20 nm thick VSe_2 nanosheet with a crossover field of about 0.5 T under a magnetic field of 9 T at 1.9 K (Figure S13b). The linear MR in all VSe_2 nanosheets, regardless of their thickness, show no tendency to saturate under the magnetic field up to 15 T at low temperatures below T_{CDW} (Figures 3a and S10a,d,g). The unusual nonsaturating linear MR can mainly be explained in quantum model or classical model.[43,44] The absence of quantum oscillation at high field and the large carrier concentration (3×10^{21} m^{-3}, 1.9 K, obtained from Hall effect in Figure S11e) in VSe_2 nanosheet suggest that the system is far from reaching the quantum limit to condensate all the carriers into the lowest Landau level.[45] As a consequence, the quantum model cannot be applied to VSe_2 since VSe_2 is a metal without Dirac-cone topological surface state.[46] Classical model can be used to explain the linear MR in VSe_2 in which large spatial conductivity fluctuations produce a linear MR.[44] Given the high-quality single-crystal of VSe_2 nanosheets and thickness dependence of MR, defects and surface induced mobility fluctuations would not be the origin of linear MR in as-grown VSe_2 nanosheets, which will lead to Kondo or weak localization effect with negative but not positive MR at low magnetic fields.[33,34] Based on the fact that linear MR only appears in CDW state of VSe_2 nanosheets at temperatures below T_{CDW} (Figures 3 and S10), and the MR and carrier mobility are strongly correlated consistent with the Parish−Littlewood model (Figure S11f),[44,47] CDW induced mobility fluctuations or strong scattering at the hot spots of Fermi surface could be the origin of the linear MR in VSe_2 nanosheets.[48,49] Both the linear MR and CDW show the same dependence on temperature and thickness. As temperature increases, linear MR disappears at $T = T_{CDW}$ and ordinary MR emerges at $T > T_{CDW}$ (Figures 3b,c, and S10b,e,h). Linear MR is large in thick VSe_2 nanosheets with strong CDW (Figures 3a, S13a,b), since the thick samples favor the 3D nesting and thus enhanced CDW.[29,30,32] When CDW is suppressed in VSe_2 nanosheets with reduced thickness, the linear MR also becomes weak (Figure 3a).

DOI: 10.1021/acs.nanolett.9b01412
Nano Lett. 2019, 19, 4551−4559

All the MRs at different temperatures except at T_{CDW} can be well fitted with the two-band model.[31] The two-band transport behavior, particularly in thin VSe_2 nanosheets (e.g., 9.6 and 4.6 nm), is further verified by the noncollapsed Kohler's plots in which the MR ratio is plotted as a function of $H/\rho_{xx}(0)$, as shown in Figure 3e,f. If only one kind of carrier with the same scattering time τ dominates the transport behavior, all curves of Kohler's plot will collapse into one curve.[50] The 28 nm thick VSe_2 nanosheet behaves more like single-band transport as the Kohler's plot collapses shown in Figure 3d. However, the Hall resistivities for VSe_2 nanosheets with different thickness at different temperatures show an almost the same linear behavior (Figure S11a−c), indicating that the two-band transport may come from mobility fluctuations due to different kinds of electrons.[51] No anomalous Hall effect is observed, which suggests no intrinsic ferromagnetic order occurs in VSe_2 even when the thickness is thinned down to 4.6 nm. The lack of ferromagnetic ground state in the few-layer VSe_2 nanosheet is due to the large thickness, as the ferromagnetism is only salient in monolayer VSe_2 and diminishes rapidly with increasing thickness.[12] The ferromagnetic order may also be suppressed by the competing strong CDW order and CDW pseudogap in VSe_2.[52−55]

When the thickness of VSe_2 nanosheet is reduced down to 4.6 nm, a sharp dip is observed in MR curves at around zero magnetic field at 1.9 K and can persist at temperatures up to 10 K (Figures 3a, S10g). This dip is completely suppressed when the magnetic field reaches to 2 T or even higher. It is a typical signature of WAL, which emerges at low temperatures when the phonon scattering is suppressed with the elastic scattering and the phase coherence remained in the presence of SOC.[15] Figure 4a shows the magnetoconductance at temperatures from 1.9 to 10 K. The cusps at different temperatures under the magnetic field below 2 T can be well fitted to the theory of Hikami, Larkin and Nagaoka (HLN)[56] (Figure 4b),

$$\Delta\sigma(B) = \sigma_{xx}(B) - \sigma_{xx}(0) = -\frac{e^2}{\pi h}\left[\frac{1}{2}\psi\left(\frac{1}{2}+\frac{B_\phi}{B}\right) - \frac{1}{2}\ln\left(\frac{B_\phi}{B}\right) - \psi\left(\frac{1}{2}+\frac{B_\phi + B_{SO}}{B}\right) + \ln\left(\frac{B_\phi + B_{SO}}{B}\right) - \frac{1}{2}\psi\left(\frac{1}{2}+\frac{B_\phi + 2B_{SO}}{B}\right) + \frac{1}{2}\ln\left(\frac{B_\phi + 2B_{SO}}{B}\right)\right] \quad (4)$$

where $B_\phi = \frac{\hbar}{4De\tau_\phi} = \frac{\hbar}{4el_\phi^2}$, $B_{so} = \frac{\hbar}{4De\tau_{SO}} = \frac{\hbar}{4el_{SO}^2}$, $\psi(x)$ is the digamma function, B_ϕ is the dephasing magnetic field, determined by the phase coherence time τ_ϕ ,or phase coherence length l_ϕ, and B_{SO} is the spin−orbit scattering field, determined by the spin−orbit scattering time τ_{SO} or spin−orbit scattering length l_{SO}. Using this 2D HLN model, the dephasing magnetic field B_ϕ and the spin−orbit scattering field B_{SO} can be extracted. The B_ϕ and B_{SO} at different temperatures extracted by fitting the magnetoconductance using the HLN theory are shown in Figure 4c. The temperature-dependence of B_ϕ shows a power law relationship, $B_\phi \propto T^p$, while B_{SO} is temperature independent.[23] For Nyquist e−e interaction-dominated dephasing, the dephasing magnetic field B_ϕ is linearly dependent on the temperature ($p = 1$), while for e−ph interactions dominated dephasing, the value of p should be 2−4.[17,27] The linear temperature dependence of B_ϕ in Figure 4c and the inverse square root temperature dependence of l_ϕ in Figure 4d indicate that e−e interactions are the dominant source of electron dephasing. The phase coherence length l_ϕ increases with decreasing temperature in a power law dependence (−1/2), while the spin−orbit scattering length l_{SO} keeps constant, leading to the increase of the magnitude of negative magnetoconductance during lowering temperature down to 1.9 K (Figure 4a,d). At 1.9 K, the phase coherence length l_ϕ (∼50 nm) is quite larger than the spin−orbit scattering length l_{SO} (∼17 nm), which means $\frac{\tau_{SO}}{\tau_\phi} < 1$, leading to the positive MR and the WAL effect.

Typically, the e−ph interactions are the dominant dephasing processes in three dimensions, while e−e interactions dominate in two dimensions.[27] The WAL effect is the intrinsic properties of the high quality ultrathin VSe_2 and can only be observed in the sub-5 nm thick few-layered VSe_2 nanosheets at temperatures below 10 K, where quantum confinement effect makes the 3D electronic band structure of VSe_2 transition to a quasi-2D one (Figure S12).[54] Moreover, the phase coherence length l_ϕ extracted from the HLN fit below 10 K is much larger than the VSe_2 nanosheet thickness d and much smaller than the channel width W ($W \gg l_\phi > l_{SO} \gg d$), indicating a 2D transport and the observation of WAL effect due to spin−orbit scattering in phase-coherent transport process ($l_\phi > l_{SO}$). The WAL effect in VSe_2 is not so robust as that in topological insulators (TI, such as Bi_2Se_3, Bi_2Te_3, etc.).[57] This is probably due to the moderately weak SOC in VSe_2 because of the small atomic number Z of V ($Z = 23$) and Se ($Z = 34$). The reason for observation of WAL effect in VSe_2 is the successful reduction of its thickness down to sub-5 nm and high quality of the sample. If the sublimed-salt-assisted CVD growth method is further improved, monolayer VSe_2 will be obtained, which will be an intrinsically valley-polarized material with the unique intrinsic ferromagnetic properties and SOC.[13,14] This might be a platform to study the novel physical properties, such as spintronics, valleytronics, anomalous valley Hall effect, and many-body physics.

In conclusion, we have developed a sublimed-salt-assisted CVD method to prepare high-quality VSe_2 nanosheets with controllable thickness down to few layers (2.48 nm, ∼4L). The growth temperature can be greatly lowered down to 400 °C owning to the sublimed-salt. The as-grown few-layer VSe_2 nanosheets were characterized as high-quality 1T phase single crystals without salt contamination. Thickness-dependent transport demonstrates that apparent nonsaturated linear MR is observed in CDW state thick (>9.6 nm) VSe_2 nanosheets, probably resulting from CDW-induced scattering at the hot spots of Fermi surface, while nonsaturated quadratic MR along with WAL effect appear in 4.6 nm thick (∼7L) VSe_2 nanosheets at the temperature below 10 K. As the thickness of VSe_2 nanosheets decreases, the CDW is suppressed, as well as the linear MR. The WAL effect can be perfectly fitted by the Hikami−Larkin−Nagaoka (HLN) equation. The linear temperature dependence of B_ϕ indicates the e−e interactions dominant dephasing mechanism. At 1.9 K, the phase coherence length l_ϕ is ∼50 nm, and the spin−orbit scattering length l_{SO} is ∼17 nm. Quantum confinement in the 4.6 nm thick VSe_2 nanosheet leads to the quasi-2D transport and thus the observation of WAL effect in the presence of intrinsic SOC demonstrated by $l_\phi > l_{SO}$ at low temperature. Moreover, the low-temperature upturn in resistivity arises due to e−e interactions in the 4.6 nm thick VSe_2 nanosheets. No signature of ferromagnetic ordering is observed in all the VSe_2

DOI: 10.1021/acs.nanolett.9b01412
Nano Lett. 2019, 19, 4551−4559

nanosheets even for the 4.6 nm thick nanosheet from room temperature down to 1.9 K. The availability of high-quality few-layered VSe_2 nanosheets and the observed WAL effect, a hallmark of 2D transport in the presence of SOC, offer an unprecedented opportunity for future applications in 2D spintronics and valleytronics.

NOTE: During the development of this manuscript, a paper appeared that demonstrated a similar method using NH_4Cl as the growth promoter for growing TiS_2, VS_2, and SnS_2.[58] However, the pure metals instead of metal oxides were used as metal precursors, and the reaction process is quite different from our method. The water in the metal/NH_4Cl mixture is detrimental to the growth. While our V_2O_5/NH_4Cl precursor is stable in air and immune to moisture.

Methods. *CVD Growth of VSe_2 Nanosheets.* The VSe_2 nanosheets were grown in a three-zone tube furnace. The vanadium precursor (well-ground mixture of vanadium pentoxide V_2O_5 and sublimed-salt NH_4Cl, wt 1:20, 10 mg) was placed in a quartz boat, and a clean growth substrate (sapphire, SiO_2/Si, glass, and polyimide (PI) etc.) was placed on the boat facedown above the vanadium precursor, which were loaded in the center of quartz tube. Selenium shots (100 mg) in another quartz boat were placed upstream in the quartz tube. After flushing the quartz tube with a mixture of H_2/Ar (1:9, v/v) for 10 min, the furnace was ramped up to 400−500 °C in 10 min with H_2/Ar carrier gas at a flow rate of 100 sccm (standard cubic centimeters per minute). After holding at 400−500 °C for 20 min, the furnace was cooled down to room temperature naturally.

Transfer of VSe_2 Nanosheets to Target Substrates. Due to the vertical standing of VSe_2 nanosheets on growth substrates, the VSe_2 nanosheets can be easily transferred to target substrates, such as SiO_2/Si, and TEM copper grid, by a face-to-face transfer method developed by Q. Q. Ji et al.[59] This transfer method is very simple and effective and can be finished in a few seconds without introducing polymer residues and other contaminants. It minimizes the air exposure and guarantees the high quality of the VSe_2 nanosheets.

Sample Characterizations. The morphology of the as-grown VSe_2 nanosheet was characterized by optical microscope (Olympus BX51-SC30) and SEM (Hitachi S-4800, acceleration voltage of 10 kV, EDS 15 kV). The thickness of VSe_2 nanosheet was determined by an atomic force microscope (AFM, Digital Instruments Nanoscope IIIa and Dimension edge, Bruker) operated in tapping mode. TEM characterization was performed using a JEM-2100F, JEOL, operating at 200 kV and equipped with an EDS system, and HAADF-STEM (JEOL JEM-ARM200F; acceleration voltage of 80 kV). Raman spectra were collected from VSe_2 nanosheets using a confocal Raman imaging microscope (WITec alpha 300R) with a 532 nm laser as the excitation source. XPS was collected by using an ESCALAB 250Xi (Thermo Fisher Scientific) spectrometer. XRD scans were collected using a Bruker D2 phaser PHASER diffractometer with Cu−Kα radiation (λ = 1.54184 Å) operating at 30 kV and 10 mA at room temperature.

Device Fabrication and Transport Measurements. The as-grown VSe_2 nanosheets were transferred to a precleaned SiO_2/Si substrate using the face-to-face transfer method. A 300 nm thick poly(methyl methacrylate) (PMMA950, A5) film was deposited by spin coating at 4000 rpm for 60 s and then was baked at 180 °C for 60 s. Hall bar devices were fabricated by a standard electron beam lithography technique (Raith 150), followed by electron beam evaporation of Ti/Au (5/60 nm) electrodes. All transport measurements were performed in a Physical Property Measurement System (PPMS, Quantum Design Inc.) using the resistivity option with AC drive mode. During the $\rho-T$ measurements, the cooling/warming rate was 2 K/min. In order to measure the WAL effect, freshly grown, high quality sub-5 nm thick samples were necessary, and when needed, they were stored in dark and minimum air exposure to reduce photo-oxidation of VSe_2.

■ ASSOCIATED CONTENT

Supporting Information

The Supporting Information is available free of charge on the ACS Publications website at DOI: 10.1021/acs.nanolett.9b01412.

Sublimed-salt-assisted CVD growth of VSe_2 nanosheets, oxidation of VSe_2, optical images, SEM, TEM, XPS, device optical images and additional data, and VSe_2 band structure (PDF)

■ AUTHOR INFORMATION

Corresponding Author

*E-mail: lhbao@iphy.ac.cn. Tel: +86-10-82649662.

ORCID

Hongtao Liu: 0000-0003-0500-7204
Lihong Bao: 0000-0002-2942-892X
Junjie Li: 0000-0002-1508-9891
Changzhi Gu: 0000-0002-2689-2807
Shixuan Du: 0000-0001-9323-1307
Hong-Jun Gao: 0000-0002-6766-0623

Author Contributions

#H.L. and L.B. contributed equally to this work. H.-J.G. conceived the idea and supervised the overall research. H.T.L. and L.H.B. designed and performed the experiments. H.T.L. together with B.Y.C. and C.M.S. synthesized the VSe_2 nanosheets and performed the structural analysis. H.T.L. together with Z.Z. and L.H.B. fabricated the devices and carried out low-temperature transport measurements. H.F.Y., J.J.L., and C.Z.G. helped the device fabrication. R.Z.Z. and S.X.D. contributed to the DFT calculations. H.T.L. together with L.H.B., Z.Z., C.B., R.S.M., and L.M.W. analyzed the results. H.T.L. and L.H.B. wrote the paper, and all of the authors contributed to the preparation of the manuscript.

Notes

The authors declare no competing financial interest.

■ ACKNOWLEDGMENTS

The authors would like to thank Prof. Min Ouyang from University of Maryland for the valuable discussions and suggestions. This work was supported by National Key Research & Development Projects of China (Grant No. 2016YFA0202300, 2018FYA0305800), National Natural Science Foundation of China (Grant No. 61674170, 61888102), Strategic Priority Research Program of Chinese Academy of Sciences (CAS, Grant No. XDB30000000, XDB28000000), and Youth Innovation Promotion Association of CAS (20150005).

■ REFERENCES

(1) Soumyanarayanan, A.; Reyren, N.; Fert, A.; Panagopoulos, C. Emergent Phenomena Induced by Spin-Orbit Coupling at Surfaces and Interfaces. *Nature* **2016**, *539* (7630), 509−517.

DOI: 10.1021/acs.nanolett.9b01412
Nano Lett. 2019, 19, 4551−4559

(2) Xu, X.; Yao, W.; Xiao, D.; Heinz, T. F. Spin and Pseudospins in Layered Transition Metal Dichalcogenides. *Nat. Phys.* **2014**, *10* (5), 343−350.
(3) Yuan, H.; Bahramy, M. S.; Morimoto, K.; Wu, S.; Nomura, K.; Yang, B.-J.; Shimotani, H.; Suzuki, R.; Toh, M.; Kloc, C.; Xu, X.; Arita, R.; Nagaosa, N.; Iwasa, Y. Zeeman-Type Spin Splitting Controlled by an Electric Field. *Nat. Phys.* **2013**, *9* (9), 563−569.
(4) Premasiri, K.; Radha, S. K.; Sucharitakul, S.; Kumar, U. R.; Sankar, R.; Chou, F.-C.; Chen, Y.-T.; Gao, X. P. A. Tuning Rashba Spin-Orbit Coupling in Gated Multilayer InSe. *Nano Lett.* **2018**, *18* (7), 4403−4408.
(5) Premasiri, K.; Gao, X. P. A. Tuning Spin-Orbit Coupling in 2D Materials for Spintronics: A Topical Review. *J. Phys.: Condens. Matter* **2019**, *31* (19), 193001.
(6) Cao, T.; Wang, G.; Han, W.; Ye, H.; Zhu, C.; Shi, J.; Niu, Q.; Tan, P.; Wang, E.; Liu, B.; Feng, J. Valley-Selective Circular Dichroism of Monolayer Molybdenum Disulphide. *Nat. Commun.* **2012**, *3*, 887.
(7) Xiao, D.; Liu, G.-B.; Feng, W.; Xu, X.; Yao, W. Coupled Spin and Valley Physics in Monolayers of MoS_2 and Other Group-VI Dichalcogenides. *Phys. Rev. Lett.* **2012**, *108* (19), 196802.
(8) Zeng, H.; Dai, J.; Yao, W.; Xiao, D.; Cui, X. Valley Polarization in MoS_2 Monolayers by Optical Pumping. *Nat. Nanotechnol.* **2012**, *7* (8), 490−493.
(9) Mak, K. F.; He, K. L.; Shan, J.; Heinz, T. F. Control of Valley Polarization in Monolayer MoS_2 by Optical Helicity. *Nat. Nanotechnol.* **2012**, *7* (8), 494−498.
(10) Ma, Y.; Dai, Y.; Guo, M.; Niu, C.; Zhu, Y.; Huang, B. Evidence of the Existence of Magnetism in Pristine VX_2 Monolayers (X = S, Se) and Their Strain-Induced Tunable Magnetic Properties. *ACS Nano* **2012**, *6* (2), 1695−1701.
(11) Xu, K.; Chen, P.; Li, X.; Wu, C.; Guo, Y.; Zhao, J.; Wu, X.; Xie, Y. Ultrathin Nanosheets of Vanadium Diselenide: A Metallic Two-Dimensional Material with Ferromagnetic Charge-Density-Wave Behavior. *Angew. Chem., Int. Ed.* **2013**, *52* (40), 10477−10481.
(12) Bonilla, M.; Kolekar, S.; Ma, Y.; Diaz, H. C.; Kalappattil, V.; Das, R.; Eggers, T.; Gutierrez, H. R.; Manh-Huong, P.; Batzill, M. Strong Room-Temperature Ferromagnetism in VSe_2 Monolayers on van der Waals Substrates. *Nat. Nanotechnol.* **2018**, *13* (4), 289−293.
(13) Tong, W.-Y.; Gong, S.-J.; Wan, X.; Duan, C.-G. Concepts of Ferrovalley Material and Anomalous Valley Hall Effect. *Nat. Commun.* **2016**, *7*, 13612.
(14) Liu, J.; Hou, W.-J.; Cheng, C.; Fu, H.-X.; Sun, J.-T.; Meng, S. Intrinsic Valley Polarization of Magnetic VSe_2 Monolayers. *J. Phys.: Condens. Matter* **2017**, *29* (25), 255501.
(15) Bergmann, G. Weak Localization in Thin Films: A Time-of-Flight Experiment with Conduction Electrons. *Phys. Rep.* **1984**, *107* (1), 1−58.
(16) Manchon, A.; Koo, H. C.; Nitta, J.; Frolov, S. M.; Duine, R. A. New Perspectives for Rashba Spin-Orbit Coupling. *Nat. Mater.* **2015**, *14* (9), 871−882.
(17) Lee, P. A.; Ramakrishnan, T. V. Disordered Electronic Systems. *Rev. Mod. Phys.* **1985**, *57* (2), 287−337.
(18) Wang, L.; Gutierrez-Lezama, I.; Barreteau, C.; Ubrig, N.; Giannini, E.; Morpurgo, A. F. Tuning Magnetotransport in a Compensated Semimetal at the Atomic Scale. *Nat. Commun.* **2015**, *6*, 8892.
(19) Wang, Y.; Liu, E.; Liu, H.; Pan, Y.; Zhang, L.; Zeng, J.; Fu, Y.; Wang, M.; Xu, K.; Huang, Z.; Wang, Z.; Lu, H.-Z.; Xing, D.; Wang, B.; Wan, X.; Miao, F. Gate-Tunable Negative Longitudinal Magnetoresistance in the Predicted Type-II Weyl Semimetal WTe_2. *Nat. Commun.* **2016**, *7*, 13142.
(20) Naylor, C. H.; Parkin, W. M.; Gao, Z.; Kang, H.; Noyan, M.; Wexler, R. B.; Tan, L. Z.; Kim, Y.; Kehayias, C. E.; Streller, F.; Zhou, Y. R.; Carpick, R.; Luo, Z.; Park, Y. W.; Rappe, A. M.; Drndic, M.; Kikkawa, J. M.; Johnson, A. T. C. Large-Area Synthesis of High-Quality Monolayer 1T′-WTe_2 Flakes. *2D Mater.* **2017**, *4* (2), 021008.
(21) Zhang, E.; Chen, R.; Huang, C.; Yu, J.; Zhang, K.; Wang, W.; Liu, S.; Ling, J.; Wan, X.; Lu, H.-Z.; Xiu, F. Tunable Positive to Negative Magnetoresistance in Atomically Thin WTe_2. *Nano Lett.* **2017**, *17* (2), 878−885.
(22) Naylor, C. H.; Parkin, W. M.; Ping, J.; Gao, Z.; Zhou, Y. R.; Kim, Y.; Streller, F.; Carpick, R. W.; Rappe, A. M.; Drndic, M.; Kikkawa, J. M.; Johnson, A. T. C. Monolayer Single-Crystal 1T′-$MoTe_2$ Grown by Chemical Vapor Deposition Exhibits Weak Antilocalization Effect. *Nano Lett.* **2016**, *16* (7), 4297−4304.
(23) Neal, A. T.; Du, Y.; Liu, H.; Ye, P. D. Two-Dimensional $TaSe_2$ Metallic Crystals: Spin-Orbit Scattering Length and Breakdown Current Density. *ACS Nano* **2014**, *8* (9), 9137−9142.
(24) Hao, S.; Zeng, J.; Xu, T.; Cong, X.; Wang, C.; Wu, C.; Wang, Y.; Liu, X.; Cao, T.; Su, G.; Jia, L.; Wu, Z.; Lin, Q.; Zhang, L.; Yan, S.; Guo, M.; Wang, Z.; Tan, P.; Sun, L.; Ni, Z.; Liang, S.-J.; Cui, X.; Miao, F. Low-Temperature Eutectic Synthesis of $PtTe_2$ with Weak Antilocalization and Controlled Layer Thinning. *Adv. Funct. Mater.* **2018**, *28* (36), 1803746.
(25) Costanzo, D.; Jo, S.; Berger, H.; Morpurgo, A. F. Gate-Induced Superconductivity in Atomically Thin MoS_2 Crystals. *Nat. Nanotechnol.* **2016**, *11* (4), 339−344.
(26) Schmidt, H.; Yudhistira, I.; Chu, L.; Neto, A. H. C.; Oezyilmaz, B.; Adam, S.; Eda, G. Quantum Transport and Observation of Dyakonov-Perel Spin-Orbit Scattering in Monolayer MoS_2. *Phys. Rev. Lett.* **2016**, *116* (4), 046803.
(27) Lin, J. J.; Bird, J. P. Recent Experimental Studies of Electron Dephasing in Metal and Semiconductor Mesoscopic Structures. *J. Phys.: Condens. Matter* **2002**, *14* (18), R501−R596.
(28) Du, Y.; Neal, A. T.; Zhou, H.; Ye, P. D. Transport Studies in 2D Transition Metal Dichalcogenides and Black Phosphorus. *J. Phys.: Condens. Matter* **2016**, *28* (26), 263002.
(29) Terashima, K.; Sato, T.; Komatsu, H.; Takahashi, T.; Maeda, N.; Hayashi, K. Charge-Density Wave Transition of 1T-VSe_2 Studied by Angle-Resolved Photoemission Spectroscopy. *Phys. Rev. B: Condens. Matter Mater. Phys.* **2003**, *68* (15), 155108.
(30) Strocov, V. N.; Shi, M.; Kobayashi, M.; Monney, C.; Wang, X.; Krempasky, J.; Schmitt, T.; Patthey, L.; Berger, H.; Blaha, P. Three-Dimensional Electron Realm in VSe_2 by Soft-X-Ray Photoelectron Spectroscopy: Origin of Charge-Density Waves. *Phys. Rev. Lett.* **2012**, *109* (8), 086401.
(31) Toriumi, A.; Tanaka, S. Galvanomagnetic Properties of 1T-VSe_2. *Physica B+C* **1981**, *105* (1−3), 141−145.
(32) Yang, J.; Wang, W.; Liu, Y.; Du, H.; Ning, W.; Zheng, G.; Jin, C.; Han, Y.; Wang, N.; Yang, Z.; Tian, M.; Zhang, Y. Thickness Dependence of the Charge-Density-Wave Transition Temperature in VSe_2. *Appl. Phys. Lett.* **2014**, *105* (6), 063109.
(33) Cao, Q.; Yun, F. F.; Sang, L.; Xiang, F.; Liu, G.; Wang, X. Defect Introduced Paramagnetism and Weak Localization in Two-Dimensional Metal VSe_2. *Nanotechnology* **2017**, *28* (47), 475703.
(34) Barua, S.; Hatnean, M. C.; Lees, M. R.; Balakrishnan, G. Signatures of the Kondo Effect in VSe_2. *Sci. Rep.* **2017**, *7*, 10964.
(35) Sugai, S.; Murase, K.; Uchida, S.; Tanaka, S. Investigation of the Charge-Density Waves in 1T-VSe_2 by Raman Scattering. *J. Phys. Colloques* **1981**, *42* (C6), 740−742.
(36) Zhang, Z.; Niu, J.; Yang, P.; Gong, Y.; Ji, Q.; Shi, J.; Fang, Q.; Jiang, S.; Li, H.; Zhou, X.; Gu, L.; Wu, X.; Zhang, Y. Van der Waals Epitaxial Growth of 2D Metallic Vanadium Diselenide Single Crystals and their Extra-High Electrical Conductivity. *Adv. Mater.* **2017**, *29* (37), 1702359.
(37) Boscher, N. D.; Blackman, C. S.; Carmalt, C. J.; Parkin, I. P.; Prieto, A. G. Atmospheric Pressure Chemical Vapour Deposition of Vanadium Diselenide Thin Films. *Appl. Surf. Sci.* **2007**, *253* (14), 6041−6046.
(38) Yadav, C. S.; Rastogi, A. K. Electronic Transport and Specific Heat of 1T-VSe_2. *Solid State Commun.* **2010**, *150* (13−14), 648−651.
(39) Thompson, A. H.; Silbernagel, B. G. Correlated Magnetic and Transport Properties in the Charge-Density-Wave States of VSe_2. *Phys. Rev. B: Condens. Matter Mater. Phys.* **1979**, *19* (7), 3420−3426.
(40) Mutka, H.; Molinie, P. Irradiation-Induced Defects in Layered Dichalcogenides: the Case of VSe_2. *J. Phys. C: Solid State Phys.* **1982**, *15* (31), 6305−6319.

DOI: 10.1021/acs.nanolett.9b01412
Nano Lett. 2019, 19, 4551−4559

(41) Breznay, N. P.; Volker, H.; Palevski, A.; Mazzarello, R.; Kapitulnik, A.; Wuttig, M. Weak Antilocalization and Disorder-Enhanced Electron Interactions in Annealed Films of the Phase-Change Compound $GeSb_2Te_4$. *Phys. Rev. B: Condens. Matter Mater. Phys.* **2012**, *86* (20), 205302.
(42) Fuh, H.-R.; Yan, B.; Wu, S.-C.; Felser, C.; Chang, C.-R. Metal-Insulator Transition and the Anomalous Hall Effect in the Layered Magnetic Materials VS_2 and VSe_2. *New J. Phys.* **2016**, *18*, 113038.
(43) Abrikosov, A. A. Quantum Magnetoresistance. *Phys. Rev. B: Condens. Matter Mater. Phys.* **1998**, *58* (5), 2788−2794.
(44) Parish, M. M.; Littlewood, P. B. Non-Saturating Magnetoresistance in Heavily Disordered Semiconductors. *Nature* **2003**, *426* (6963), 162−165.
(45) Abrikosov, A. A. Quantum Linear Magnetoresistance. *Europhys. Lett.* **2000**, *49* (6), 789−793.
(46) Tang, H.; Liang, D.; Qiu, R. L. J.; Gao, X. P. A. Two-Dimensional Transport-Induced Linear Magneto-Resistance in Topological Insulator Bi_2Se_3 Nanoribbons. *ACS Nano* **2011**, *5* (9), 7510−7516.
(47) Wang, Z. H.; Yang, L.; Li, X. J.; Zhao, X. T.; Wang, H. L.; Zhang, Z. D.; Gao, X. P. A. Granularity Controlled Nonsaturating Linear Magnetoresistance in Topological Insulator Bi_2Te_3 Films. *Nano Lett.* **2014**, *14* (11), 6510−6514.
(48) Sinchenko, A. A.; Grigoriev, P. D.; Lejay, P.; Monceau, P. Linear Magnetoresistance in the Charge Density Wave State of Quasi-Two-Dimensional Rare-Earth Tritellurides. *Phys. Rev. B: Condens. Matter Mater. Phys.* **2017**, *96* (24), 245129.
(49) Feng, Y.; Wang, Y.; Silevitch, D. M.; Yan, J. Q.; Kobayashi, R.; Hedo, M.; Nakama, T.; Onuki, Y.; Suslov, A. V.; Mihaila, B.; Littlewood, P. B.; Rosenbaum, T. F. Linear Magnetoresistance in the Low-Field Limit in Density-Wave Materials. *Proc. Natl. Acad. Sci. U. S. A.* **2019**, *116*, 11201.
(50) Ziman, J. M. *Electrons and Phonons*; Oxford University Press: 1960.
(51) Hou, Z.; Yang, B.; Wang, Y.; Ding, B.; Zhang, X.; Yao, Y.; Liu, E.; Xi, X.; Wu, G.; Zeng, Z.; Liu, Z.; Wang, W. Large and Anisotropic Linear Magnetoresistance in Single Crystals of Black Phosphorus Arising From Mobility Fluctuations. *Sci. Rep.* **2016**, *6*, 23807.
(52) Duvjir, G.; Choi, B. K.; Jang, I.; Ulstrup, S.; Kang, S.; Trinh Thi, L.; Kim, S.; Choi, Y. H.; Jozwiak, C.; Bostwick, A.; Rotenberg, E.; Park, J.-G.; Sankar, R.; Kim, K.-S.; Kim, J.; Chang, Y. J. Emergence of a Metal-Insulator Transition and High-Temperature Charge-Density Waves in VSe_2 at the Monolayer Limit. *Nano Lett.* **2018**, *18* (9), 5432−5438.
(53) Chen, P.; Pai, W. W.; Chan, Y. H.; Madhavan, V.; Chou, M. Y.; Mo, S. K.; Fedorov, A. V.; Chiang, T. C. Unique Gap Structure and Symmetry of the Charge Density Wave in Single-Layer VSe_2. *Phys. Rev. Lett.* **2018**, *121* (19), 196402.
(54) Feng, J.; Biswas, D.; Rajan, A.; Watson, M. D.; Mazzola, F.; Clark, O. J.; Underwood, K.; Markovic, I.; McLaren, M.; Hunter, A.; Burn, D. M.; Duffy, L. B.; Barua, S.; Balakrishnan, G.; Bertran, F.; Le Fevre, P.; Kim, T. K.; van der Laan, G.; Hesjedal, T.; Wahl, P.; King, P. D. C. Electronic Structure and Enhanced Charge-Density Wave Order of Monolayer VSe_2. *Nano Lett.* **2018**, *18* (7), 4493−4499.
(55) Adolfo, O.; Fumega, V. P. Absence of Ferromagnetism in VSe_2 Caused by its Charge Density Wave Phase. arXiv:1804.07102, 2018.
(56) Hikami, S.; Larkin, A. I.; Nagaoka, Y. Spin-Orbit Interaction and Magnetoresistance in the Two Dimensional Random System. *Prog. Theor. Phys.* **1980**, *63* (2), 707−710.
(57) Kim, Y. S.; Brahlek, M.; Bansal, N.; Edrey, E.; Kapilevich, G. A.; Iida, K.; Tanimura, M.; Horibe, Y.; Cheong, S.-W.; Oh, S. Thickness-Dependent Bulk Properties and Weak Antilocalization Effect in Topological Insulator Bi_2Se_3. *Phys. Rev. B: Condens. Matter Mater. Phys.* **2011**, *84* (7), 073109.
(58) Gao, Z.; Ji, Q.; Pin-Chun, S.; Han, Y.; Leong, W. S.; Mao, N.; Zhou, L.; Su, C.; Niu, J.; Ji, X.; Goulamaly, M. M.; Muller, D. A.; Li, Y.; Kong, J. In Situ-Generated Volatile Precursor for CVD Growth of a Semimetallic 2D Dichalcogenide. *ACS Appl. Mater. Interfaces* **2018**, *10* (40), 34401−34408.
(59) Ji, Q.; Li, C.; Wang, J.; Niu, J.; Gong, Y.; Zhang, Z.; Fang, Q.; Zhang, Y.; Shi, J.; Liao, L.; Wu, X.; Gu, L.; Liu, Z.; Zhang, Y. Metallic Vanadium Disulfide Nanosheets as a Platform Material for Multifunctional Electrode Applications. *Nano Lett.* **2017**, *17* (8), 4908−4916.

DOI: 10.1021/acs.nanolett.9b01412
Nano Lett. 2019, 19, 4551−4559